Thoracic Cancer
Open Access
Thoracic Cancer ISSN 1759-7706

ORIGINAL ARTICLE

Biodistribution of andrographolide to assess the interior-exterior relationship between the lung and intestine using microPET

Qi Zhang & Qingxin Cui

College of Pharmacy, State Key Laboratory of Medicinal Chemical Biology, Tianjin Key Laboratory of Molecular Drug Research, Nankai University, Tianjin, China

Keywords
Andrographolide; enteritidis; interior-exterior relationship; pneumonia; positron emission tomography.

Correspondence
Qingxin Cui, College of Pharmacy, State Key Laboratory of Medicinal Chemical Biology, Tianjin Key Laboratory of Molecular Drug Research, Nankai University, Tianjin 300353, China.
Tel.\Fax: +86 22 23505259
Email: cuiqingxin@nankai.edu.cn

Received: 4 August 2020;
Accepted: 11 September 2020.

doi: 10.1111/1759-7714.13682

Thoracic Cancer **11** (2020) 3365–3374

Abstract

Background: One classic traditional Chinese medicine theory is that the "lung and intestine are exterior-interiorly related"; however, this has not been confirmed experimentally. The aim of this study was to provide a biological basis for the theory by measuring the tissue distribution of andrographolide.

Methods: Acute pneumonia was induced in a mouse model by repeated stimulation with lipopolysaccharide. The distribution of andrographolide in mice was observed by positron emission tomography (PET) imaging with [^{18}F]-labeled andrographolide, and changes in the in vivo distribution before and after modeling were compared. Subsequently, the consistency of pathological changes in lung and intestine was confirmed by observation of pathological sections. Finally, the results were verified by cytokine detection.

Results: The value of organ uptake, pathological changes and inflammatory factor expression of the lung and intestine were consistent. The concentration of andrographolide in the lung and intestine increased significantly, and was confirmed by pathology and enzyme-linked immunosorbent assays (ELISA).

Conclusions: Micro-positron emission tomography (microPET) can be used to visually observe the distribution of medicinal ingredients in vivo, and [^{18}F]-andrographolide can be used as a tool to assess the interior-exterior relationship between the lung and intestine.

Introduction

The idea that the "lung and intestine are exterior-interiorly related" originated from "Huang Di Nei Jing", one of the important basic theories of Chinese medicine.[1] This ancient Chinese medicine theory means that pathological changes in the lung and intestine reflect each other.[2] These two organs also influence each other pathologically, and the pathological state of the lung affects the function of the intestine. Pulmonary resistance and pulmonary compliance have been reported to be closely related to rectal resting pressure in the asthmatic rat model, while rectal resting pressure was correlated with pulmonary resistance in the rat model of constipation.[3] For example, inflammation in the lung can cause abnormal bowel function and constipation, and problems in the physiological processes of the lung can lead to diarrhea. The outbreak of the new coronavirus pneumonia (COVID-19) in Wuhan, Hubei Province, China in December 2019 has attracted great attention at home and abroad, posing a major challenge to clinical treatment.[4,5] Pneumonia induced by COVID-19 infection is mainly characterized by fever, weakness and dry cough, and a small number of patients also experience nasal congestion, runny nose, diarrhea and other symptoms.[6,7] Symptoms associated with the respiratory and digestive systems are of great interest to us.[5,8,9] The Chinese medicine method focuses on the relationship between the lung and intestine during treatment and achieves the purpose of whole body treatment by rational use of traditional Chinese medicine (TCM).[10] However, there are no scientific methods or suitable compounds to confirm the correlation

between the physiological function and pathological changes in the lung and intestine.

Andrographolide (AG) is the main effective ingredient of *Andrographis paniculata* (*Burm. f.*) Nees, which has the effect of dispelling heat and detoxification, reducing inflammation and relieving pain, and has a special effect on bacterial and viral respiratory tract infections and dysentery.[11] As an important raw material, AG has been made into tablets, capsules, drop pills and other dosage forms that are widely used in upper respiratory tract infections, acute pharyngitis, tonsillitis, bacterial dysentery, and gastroenteritis.[12,13] Because of the specific distribution and multitarget nature of AG in vivo, it is possible to use it to study the functional relationship between the lung and intestine.

Positron emission tomography (PET) is a new noninvasive nuclear medical imaging technique for measuring biological functions.[14] Initially, it was used for human research, especially blood flow and glucose metabolism in the heart and brain.[15] With research advancements, MicroPET has been used in clinical analysis to observe the occurrence and development of cancer,[16] epilepsy[17] and neurological diseases[18] and to guide other new developments.[19] One promising application is that MicroPET can be used to study the mechanism of action of drugs and evaluate the effect of drugs through the establishment of different animal models.[20] It can also promote the results of animal experiments to clinical practice, providing an important experimental basis for the further use of clinical pharmacokinetics and clinical pharmacodynamics.[21] This development has important implications for laboratory and clinical trials.[22] In the field of pharmacokinetics, the use of MicroPET has become more widespread.[23] MicroPET can observe the distribution of drugs in organs and tissues in real time, providing a key technique for studying correlations between the lung and intestine.

In this study, we utilized the acute pneumonia mouse model and labeled [^{18}F]- AG and then applied MicroPET to study the distribution of [^{18}F]-AG in mice, collecting dynamic data for statistical analysis. Pathological and inflammatory factor analysis were then used to confirm that the lung and intestine reflected mutual responses. It was confirmed that AG could be used as a tool to study the interaction between the lung and intestine, providing a scientific basis for traditional Chinese medicine (TCM) theory.

Methods

Reagents and chemicals

AG was purchased from Shilan S&T (Tianjin, China). P-toluene sulfonyl chloride, pyridine, and tetrahydrofuran were purchased from Aladdin (Shanghai, China). The QMA and C_{18} chromatographic columns were purchased from Waters Corporation (Milford, MA, U.S.A.). Kryptofix2.2.2 (K2.2.2) was purchased from ABX Corporation (Radeberg, Germany). Lipopolysaccharide (LPS) was purchased from Sigma-Aldrich Corporation (St. Louis, MO, USA). Human tumor necrosis factor alpha (TNF-α) was purchased from PeproTech (Rocky Hill, NJ, USA). The ELISA kits (TNF-α, IL-8) were purchased from Biosource International Life Technologies Corporation (Camarillo, CA, USA). The other reagents used were of analytical purity. Double distilled water was obtained from the Millipore filtering system (Tokyo, Japan).

Synthesis of 19-Ts-AG

4-toluene sulfonyl chloride (54 mg, 0.29 mmol) dissolved in 2 mL pyridine was gradually added to a stirred solution of AG (1 g, 0.29 mmol) in 20 mL of tetrahydrofuran. The reaction mixture was allowed to stand for 48 hours at room temperature. After completion, it was purified by silica column chromatography to obtain 19-Ts-AG. The general synthetic strategy is shown in Fig 1a.

Synthesis of [^{18}F] - AG

The QMA column was rinsed with 10 mL $NaHCO_3$ solution (0.5 M) and 20 mL water for injection in the correct order and then blow dried. Next, the C_{18} column was rinsed with 10 mL methanol and 20 mL water for injection in the correct order and then blow dried. Subsequently, 1.5 mL k2.2.2 and 2 mg 19-Ts-AG dissolved in 1.2 mL anhydrous acetonitrile were added to a 10 mL vial. The [^{18}F]-water solution passed through the QMA at the pressure of helium gas and was captured by the QMA, and the measurement activity was 258 mCi. The [^{18}F]$^-$ on the QMA was rinsed into the reaction tube to bind K222 by nitrogen, and the water was then removed at a temperature of 110°C for the first time. Then, 2 mL dry acetonitrile was added to remove the water at 110°C for the second time. 19-Ts-AG was added into the column and incubated for 10 minutes at 95°C. After the reaction was completed, 8 mL ultrapure water was added to the C_{18} column. The product was eluted into the product bottle with 2 mL acetonitrile, and the measurement activity was 2.33 mCi. The stability study of [^{18}F]-AG was performed by testing the radiochemical purity after the end of synthesis.

Radiopharmaceutical quality control

Radiochemical identity and the purity of [^{18}F]-AG were assayed by ion chromatography and in-line conduct metric and g-detectors (930 Compact IC Flex; Waters). The

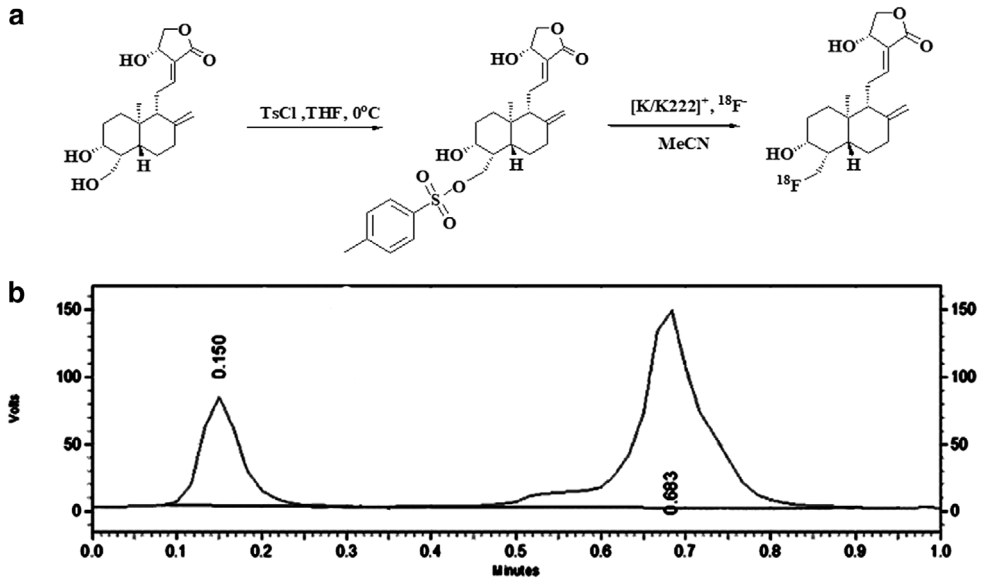

Figure 1 (**a**) The synthetic strategy of [^{18}F]-AG; (**b**) Quality control of [^{18}F]-AG.

chromatographic column was Shodex IC I-524A (4.6 × 100 mm), and the column temperature was maintained at 40°C. The mobile phase was 2.5 mM phthalic acid (pH 4.0) at a flow rate of 1.0 mL/minute.[21] The concentration of [$^{19/18}$F]-AG was assayed by a calibration curve. With silica gel (silica GF_{254}, 5 x 10 cm; Qingdao chem. Co.) as the stationary phase and methanol as the mobile phase for thin layer chromatography (TLC), radiation thin layer scanning was carried out on the plate using the [^{18}F]-AG peak (Rf = 0.683) to determine the radiochemical purity of the product (Fig 1b). A bacterial endotoxin assay was performed by Endosafe Portable Test System (Charles River) with a sensitivity of 0.05–5.0 eu/mL.

Preparation of [^{18}F]-AG

The eluted [^{18}F]-AG was collected in the tube and dried in a vacuum at 40°C. After 48 hours, [^{18}F] completely decayed to [^{19}F], and the residue was stored at 4°C for subsequent determination of anti-inflammatory activity.

Anti-inflammatory assay in vitro

The anti-inflammatory activity of [^{19}F]-AG (F-AG) was determined according to previously reported methods[24] and calculated as the ratio of firefly luciferase activity to Renilla luciferase activity (internal control).

Animal grouping and administration

Male Kunming mice, weighing 20–25 g, were purchased from the Experimental Animal Center of Cavensla (Changzhou, China). A total of 16 mice were randomly divided into two groups: the control group (Con) and the model group (Mod). Mice in the control group were fed standard food and given free access to water without any treatment. Mice in the model group were given intranasal (i.n.) LPS at 100 μL per day for three days, which induced inflammation. During the modeling period, the mice had free access to food and water. The mice were fasted for 12 hours before administration and subsequent dissection. For MicroPET imaging and biodistribution studies, mice in both groups were injected via the tail vein with 200 μL saline containing 100 μCi radioactive tracers.

MicroPET imaging and data collection

After administration of radioactive tracers, the mice were scanned with a MicroPET scanner (Focus F-120, Siemens) at 5, 15, 25, 35, 45, 55, 90, and 120 minutes under anesthesia with 1.5% to 3% isoflurane. MicroPET Manager (version 2.4.1.1, Siemens) was used to reconstruct MicroPET data using the OSEM3D/MAP algorithm (zoom factor, 2.164). The data processing software ASIProvm was used to draw the organs of each tissue as regions of interest, and the percentage of radioactive uptake concentration (μCi/mL) of each region of interest to the injection dose (100 μCi/mL) was the tissue or organ uptake ratio.

Histomorphological observations

The lung and intestinal organs of the mice were harvested and rinsed with normal saline to remove blood attached to the organs and dried with filter paper. The organ was then fixed, dehydrated and embedded in 4% paraformaldehyde and stained with hematoxylin-eosin (H&E). The histomorphological changes in tissue sections were observed under an optical microscope (Precipoint O8, Germany).

Assay of intestinal permeation

Intestinal permeability was evaluated following a modified version of Lange's method. The proximal intestine was incised at the junction with the cecum, and the fecal contents in the intestine were washed out gently with PBS. The proximal intestine and distal rectum were then ligated, and 0.2 mL of 1.5% (w/v) Evans blue (EB) in PBS was injected into the lumen of the intestine. After surgery, the mice were warmed with an incandescent lamp until they recovered from anesthesia. After 120 minutes of exposure to EB, the mice were sacrificed by cervical spine dislocation. The intestine was rapidly dissected out, and the amount of EB that had permeated into the gut wall was assayed.

The dissected intestine was opened and rinsed three times in 6 mM acetylcysteine in PBS at room temperature. The intestine was dried on filter paper at 37°C. The intestine was then weighed and incubated with 1 mL of formamide at 50°C for 24 hours. The amount of dye eluted was estimated with microplate reader (Thermo, CA, USA) at a wavelength of 655 nm. The amount of EB permeating the gut wall (μg EB/mg intestine tissue) was calculated based on the standard curve of EB in formamide.

Determination of inflammatory factors in the lung and intestine

The lung and intestinal organs of the mice were harvested and rinsed with normal saline to remove blood attached to the tissues and dried with filter paper. A triploid volume of precooled PBS was added to the organs, which was ground with a tissue homogenizer and kept at 4°C. The tissue homogenate was centrifuged at 4°C. The levels of TNF-a and IL-8 in the supernatant were then determined and the absorbance of each sample measured at 450 nm using a microplate reader (Bio-Rad Model 680, Hercules, CA, USA), following the manufacturer's instructions (Biosource International Life Technologies Corporation, Camarillo, CA, USA).

Results

Biodistribution of [^{18}F]-AG in mice

Structural identification of 19-Ts-AG

The yield of 19-Ts-AG was 39%, and the structure was characterized by ^{1}H NMR and ^{13}C NMR. ^{1}H NMR (DMSO-d6, 300 MHz) δ 0.52 (3H, s), 0.95 (3H, s), 1.14–1.26 (3H, m), 1.31–1.44 (2H, m),1.47–1.57 (1H, m), 1.63–1.75 (2H, m), 1.86 (2H, s), 2.29 (1H, d, J = 12.6 Hz), 2.41 (3H, s), 2.46 (1H, s),3.08–3.21 (1H, m), 3.88–3.99 (1H, m), 4.00–4.08 (1H, m), 4.14 (1H, d, J = 10.0 Hz), 4.32–4.42 (1H, m), 4.61 (1H, s), 4.76–4.97 (2H, m), 5.74 (1H, s), 6.45–6.70 (1H, m), 7.48 (2H, d, J = 8.0 Hz), 7.74 (2H, d, J = 8.3 Hz). ^{13}C NMR (101 MHz, $CDCl_3$) δ 14.1, 21.6, 22.9, 24.2, 25.4, 27.9, 36.7, 38.0, 39.1, 42.4, 53.9, 55.9, 65.0, 74.8, 76.5, 108.8, 128.1, 130.6, 132.5, 145.3, 146.7, 147.8, 148.4, 170.4.

Quality control

The purity of [^{18}F]-AG of all batches was greater than 98.5%, and the radiochemical purity was 100%. The mean quality control and SD of the injected [^{18}F]-AG was 12.3 ± 3.83 mg, and the activity at injection was 10.23 ± 3.75 MBq/μg. All batches were free of insoluble impurities, sterile and free of pyrogen. There were no significant changes in vital signs during the experiment.

Biodistribution of [^{18}F]-AG in mice

A typical biodistribution curve of the radiotracer from the first (five minutes) to the last MicroPET scan (120 minutes) in the mice is shown in Fig 2. As seen in Fig 2a in the control group, AG was mainly distributed in the heart, lung, stomach, liver, kidney and intestine of mice and gradually decreased with time, indicating that the drug underwent normal primary metabolism in these organs and tissues. The drug concentration in the liver increased first and then decreased, reaching a peak within 15 minutes, indicating that the liver was the main metabolic organ of AG. The drug concentrations in the muscle and brain were always at the lowest level, indicating that AG could not penetrate the muscle or blood-brain barrier.

As shown in Fig 2b, the concentrations of andrographolide in the lung and intestine were significantly higher in the model group than in the control group.

Comparing the imaging of the two groups (Fig 2c), as time went on, the radiation intensity of the lungs and intestine of mice in the model group was significantly higher than that of the control group, and the radiation intensity of mice in the model group was continuously higher than that of other tissues and organs within two hours. Therefore, the main uptake of AG was in the lung and intestine, which had specific distribution.

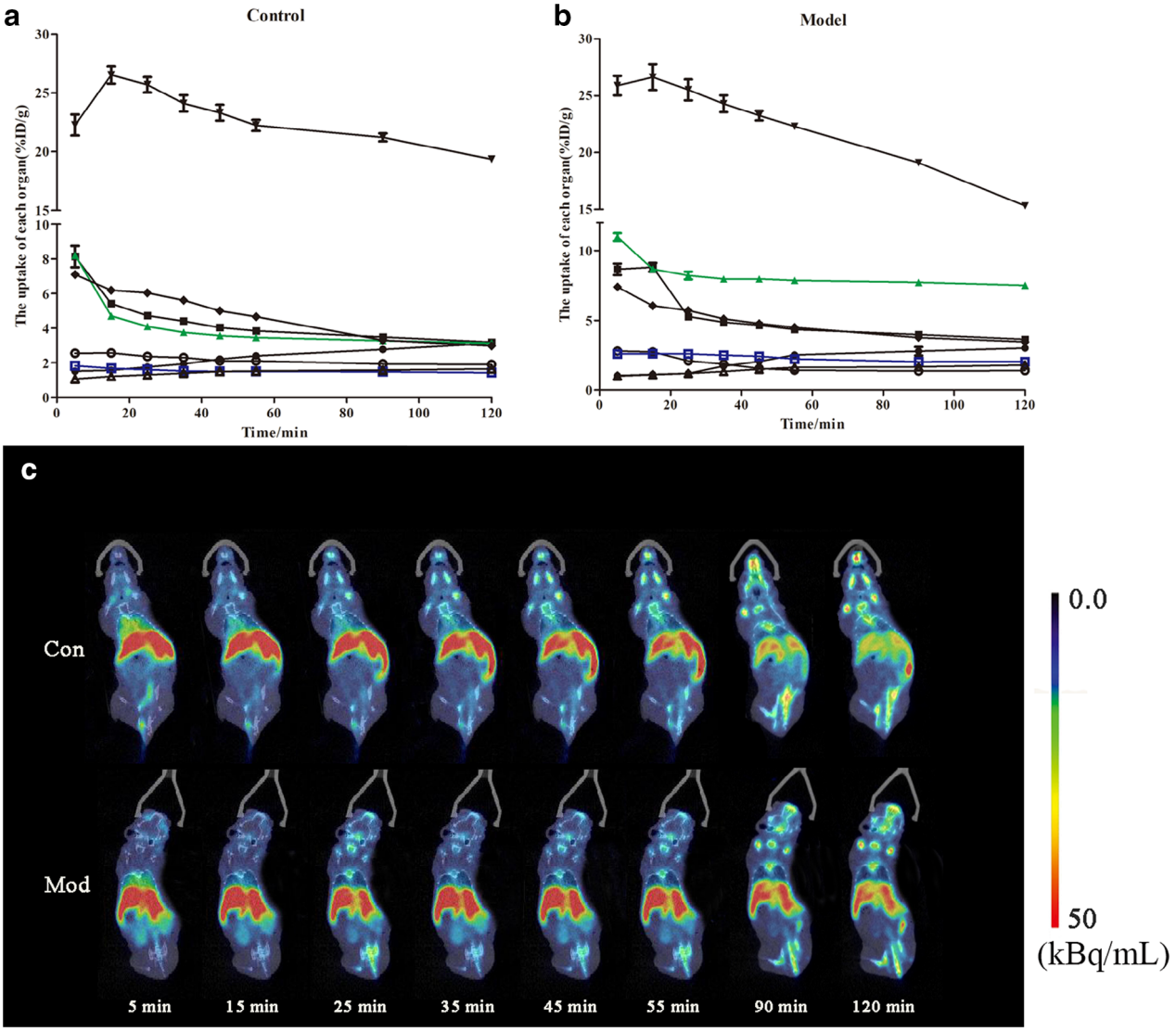

Figure 2 Biodistribution of [^{18}F]-AG. (**a**) Organ uptake (expressed as a percentage of the injected dose) for [^{18}F]-AG over time in the control group. (**b**) Organ uptake (expressed as a percentage of the injected dose) for [^{18}F]-AG over time in the model group (—●—) Brain (—■—) Heart (—▲—) Lung (—▼—) Liver (—◆—) Kidney (—○—) stomach (—□—) intestine (—△—) muscle. (**c**) Whole body biodistribution of [^{18}F]-AG over time.

NF-κB inhibitory activity of F-AG

The NF-κB inhibitory activity of F-AG was tested after complete decay of the radioactive element. F-AG and AG were respectively added to HEK 293T cells already activated by TNF-α, and its activity determined (Fig 3a). High concentrations (10^{-4} M) of F-AG and AG showed significant inhibition of NF-κB activity, which was similar to that of the positive control drug (Dex, 10 μmol/L). At medium concentrations (10^{-5} M), they also showed significant activity, while the anti-inflammatory activity of F-AG was weak at low concentrations (10^{-6} M). Due to its pharmacological action and dose dependence, F-AG has a similar anti-inflammatory activity to AG; thus, it can be used as an approximately equivalent compound to study the distribution of AG in the lung and intestine.

Changes in tissue distribution after modeling

The lungs of mice were scanned at different time points to record the radiation intensity and mapped with Prism GraphPad 5. Variation in the uptake of each organ was compared after modeling, as shown in Fig 3b. The elevation of intestine was the most significant, at two times that of the control group. The uptake of lung was also significantly increased, at 1.5 times that of the control group. Interestingly, there were no significant changes in other organs. This indicates that AG can be specifically distributed in the

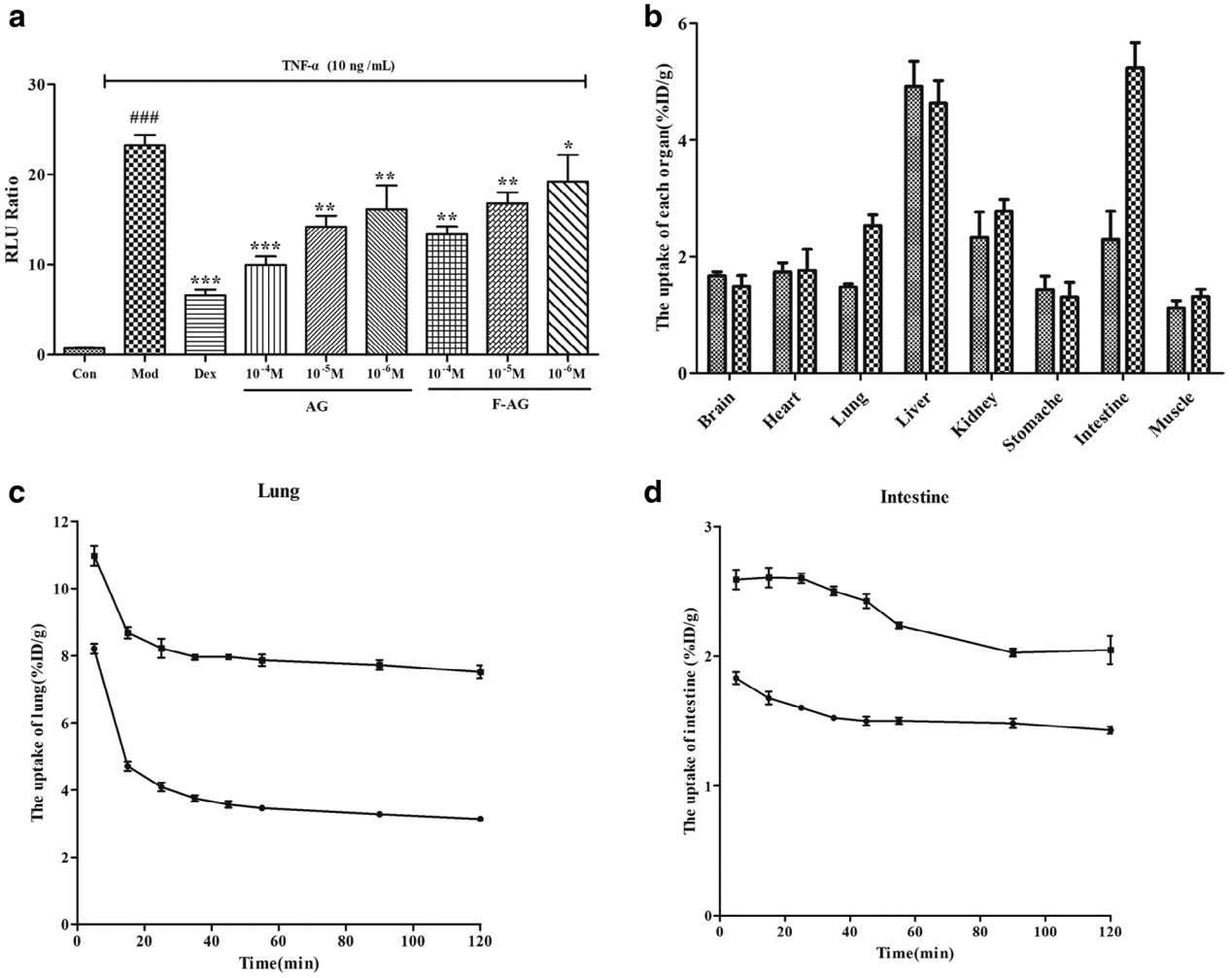

Figure 3 The uptake in organs. (**a**) Confirmation of NF-κB inhibition activity of F-AG by the luciferase reporter assay system. Each bar represents the means ± SEM, $n = 6$ per group. $^{**}P < 0.01$ versus control group; $^{***}P < 0.005$ versus control group. (**b**) Changes in the absolute value of each organ after modeling. (▩) Control (▩) Model. (**c**)The lung uptake in the control and model group. (—●—) Control (—■—) Model. (**d**) The intestine uptake in the control and model groups. (—●—) Control (—■—) Model.

lung and intestine and indicates the correlation between the lung and intestine. The lung radiation intensity of the model group was significantly higher than that of the control group, as shown in Fig 3c. The same method was then used to compare the radiation intensity of the intestine, which was again higher in the model group than in the control group (Fig 3d).

Histopathological changes of the lung

Morphology of the lung

In the control group, the lung tissue boundaries were clear and complete, the alveolar morphology was uniform, no obvious exudation or congestion was observed in the alveolar wall, the thickness of the alveolar interstitium was moderate, and there were few secretions or inflammatory cells in the bronchial lumen (Fig 4a).

In the model group, the lung tissue was severely damaged, and the borders were not clear or intact. The number of alveoli had decreased significantly, the alveolar wall was thickened, and some inflammatory cells significantly infiltrated the alveolar cavity. Epithelial detachment of the bronchial mucosa resulted in a large number of tissues, inflammatory cells, and red blood cells visible in the lumen, as shown in Fig 4b.

Inflammation of the bronchi

Compared with the control group, there was a significant difference between the model group and the control group ($P < 0.001$), and the proportion of bronchial inflammatory

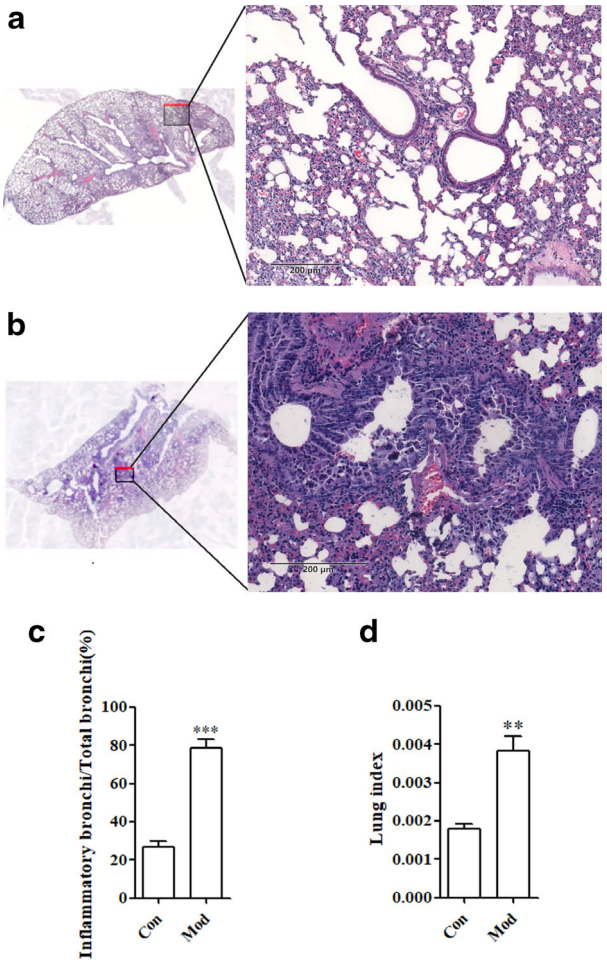

Figure 4 Histopathological changes of the lung. (**a**) H&E staining of the lung in the control group. (**b**) H&E staining of the lung in the model group. (**c**) Statistics of the proportion of injured bronchi. (**d**) Statistics of the lung index. $^{**}P < 0.01$ versus control group; $^{***}P < 0.005$ versus control group.

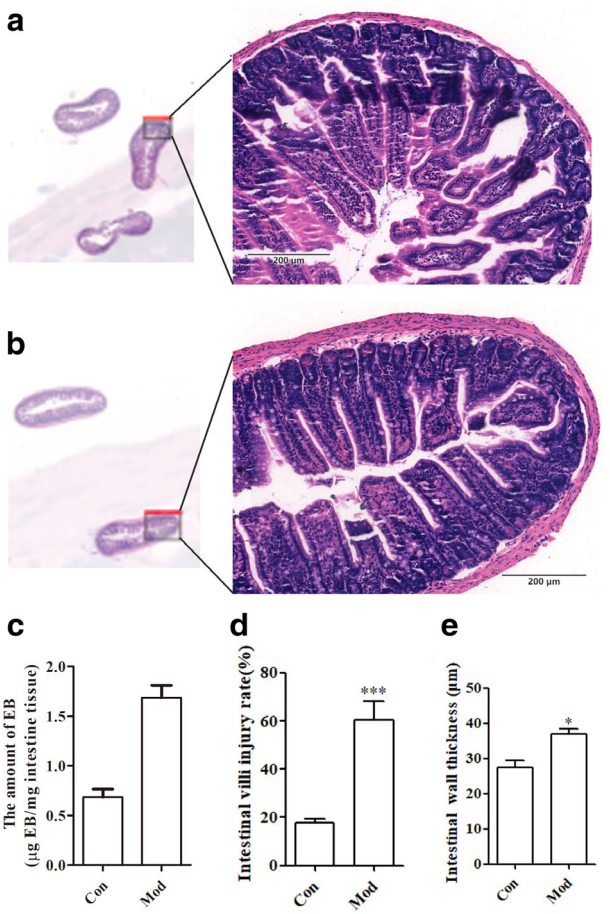

Figure 5 Histopathological changes of the intestine. (**a**) HE staining of the intestine in the control group. (**b**) HE staining of the intestine in the model group. (**c**) The permeation of EB into the gut wall from the lumen in the intestine after 120 minutes of exposure in the control and model groups. (**d**) Statistics of the proportion of injured intestinal villi. (**e**) Statistics of the thickness of the wall of the intestine. $^{*}P < 0.05$ versus control group; $^{***}P < 0.005$ versus control group.

infiltration was significantly increased, as shown in Fig 4b. This suggests that mice have fewer functioning bronchi and limited lung function.

Changes in the lung index

The lung index in the model group (Mod) was significantly higher than that in the control group (Con), with a statistically significant difference ($P < 0.001$), as shown in Fig 4c. This suggests that LPS causes inflammatory lesions in the lungs of mice, and inflammatory exudation causes weight gain in the lungs.

Histopathological changes of the intestine

Morphology of the intestine

The intestinal tissues in the control group had intact mucosa and uniform folds. There was no obvious inflammatory exudate, the vascular course was clear, and there was no obvious ulceration. The intestinal wall was uniform, and the intestinal cavity space was large. There was no significant inflammatory proliferation, glandular proliferation, or polyp formation, as shown in Fig 5a.

In the model group, the intestinal tissues of the mucosal folds disappeared, and hyperaemia and oedema were exfoliated. Mucous membrane inflammation exudates increased, and a pleomorphic shallow ulcer was formed. The intestinal wall thickened, and the lumen narrowed significantly. The glands were disorganized and had various inflammatory cell infiltrates, as shown in Fig 5b.

Changes in intestinal permeability

Compared to that in control mice, the amount of EB that had permeated into the intestinal wall increased significantly

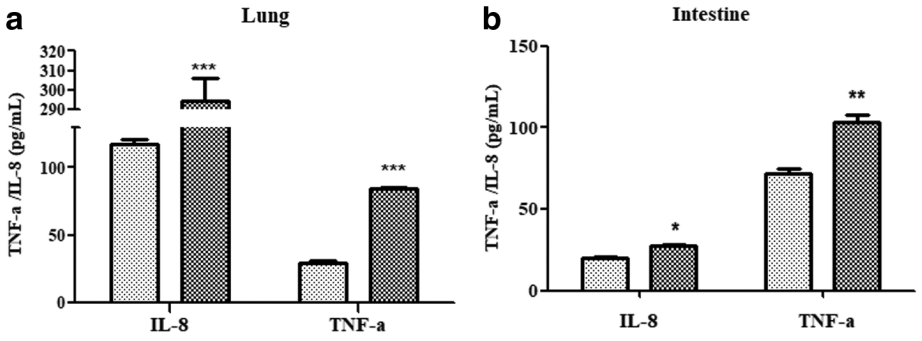

Figure 6 Assay of inflammatory factors in the lung and intestine. (**a**) Detection of inflammatory factors in the lung (▨) Con (▩) Mod. (**b**) Detection of inflammatory factors in the intestine. $^{*}P < 0.05$ versus control group; $^{**}P < 0.01$ versus control group; $^{***}P < 0.005$ versus control group.

(Fig 5c). The amount of EB in the model group was approximately twice as high as that in the control group. The mean amount of EB that had permeated into the intestinal wall in the control group was 0.685 μg/mg, while the mean amount in the model group was 1.687 μg/mg.

Pathological changes of intestinal villi

The villi morphology of the model group (Mod) and the control group (Con) changed significantly. Less than 20% of the villi were shed in the control group, while 60% of the villi were shed in the model group, as shown in Fig 5d. This indicates that LPS stimulation had a greater effect on the intestinal villi of mice.

Pathological changes in the thickness of the intestinal wall

There was a significant difference in the intestinal wall thickness between the model group (Mod) and the control group (Con) ($P < 0.001$), as shown in Fig 5e. The thickness of the intestinal wall in the model group increased significantly, indicating that LPS stimulation caused glandular hyperplasia and inflammatory thickening of the intestine.

Assay of inflammatory factors in the lung and intestine

TNF-α and IL-8 are two important inflammatory factors that trigger and participate in various inflammatory responses. The expression levels of TNF-α and IL-8 were positively correlated with the severity of lung and intestinal tissue disease and could be used as an important indicator in respiratory and digestive systems. After LPS modeling, TNF-α and IL-8 were significantly elevated in the lung and intestinal tissues of mice, as shown in Fig 6a,b.

Discussion

As a noninvasive medical imaging tool, MicroPET can reflect changes in small molecules in cells or tissues in real time, and it has been widely used in the clinical diagnosis of tumors and other medical processes.[25,26] With the development of MicroPET technology in recent years, it can be applied to the study of in vivo distribution of pharmacokinetics to visually trace labeled molecules of animals in vivo and explore drug distribution in tissues and organs.[27]

In this study, we labeled AG with [^{18}F], evaluated the anti-inflammatory activity of [^{18}F]-AG, and then used MicroPET technology to study the distribution of AG in vivo. We then observed changes in the uptake of the lung and intestine before and after modeling. The results showed that changes of the lung and intestine were consistent. This suggests that AG can be used as a suitable carrier to study correlations between the lung and intestine and that MicroPET technology can be used to observe changes in the distribution of drugs in the animal as a whole.

While observing the images, we collected dynamic data to calculate the average and maximum uptake values of radioactive substances in organs and tissues (SUV and % ID/g). According to the data, a drug time curve was drawn. Based on the drug time curve in the control group, AG was distributed in the major tissues and organs in mice, such as heart, lung, liver, kidney, stomach and intestine, which corresponded to normal metabolic processes and was consistent with the results of an existing study on the distribution of AG in vivo.[28,29] Comparing the uptake before and after, the AG concentration in the lungs and intestines of the model group increased significantly. AG showed consistency in the pathological changes of lung and intestine, which could be used to study correlations between the two organs. We then calculated the absolute value of the drug concentration difference between the control group and the model group at the same time, and compared the tissue distribution changes after administration, and observed changes in the lung and intestinal imaging at the same time interval. The results showed that the increased drug concentrations in the lung and intestine were the largest and significantly higher than that in other tissues. This result is consistent with current research,[30,31] proving the similarity of pathological and pharmacological responses between the lung and intestine and providing a

new avenue for the theoretical research of traditional Chinese medicine.

In molecular biological organ studies, LPS has been reported to significantly induce inflammatory factors, such as TNF-α and IL-8, leading to inflammatory injury of bronchi, increased lung index, decreased intestinal villi and thickening of the intestinal wall.[32] Coincidentally, it has been reported that AG can inhibit the expression of inflammatory factors, such as NO, TNF-α and IL-8, in a dose-dependent manner, thus inhibiting the inflammatory response.[33–35] This confirmed that it was appropriate to choose AG to study the correlation between the lung and intestine, laying a foundation for follow-up research on the mechanism of action and providing a new appreciation of traditional Chinese medicine theory.

Previous study had confirmed that both the lung and intestine were organs with secondary endocrine functions which could synthesize a serial of active substances when receiving signals from the internal and external environments.[36] LPS is widely used as a reference allergen to induce allergic asthma, which can cause the imbalance of CD4+ T lymphocytes, secretion of cytokines, and immune inflammation.[3] In our model of LPS-induced asthma, the expressions of immune related factors, such as TNF-α and IL-8, were changed; meanwhile, the corresponding receptors were subsequently altered in the intestine; in this way the pathological condition of lung may influence the status of the intestine.

In conclusion, a modification was made to AG by 4-toluene sulfonyl chloride followed by radio labelling with [^{18}F]. The newly synthesized probe molecule was injected into mice to compare the drug concentration in the lung and the intestine. MicroPET imaging showed that the biodistribution could be detected using this radiotracer, which provides a direct tool for future research into the connection between these two organs. These results warrant further development of MicroPET imaging to substantiate the traditional Chinese medicine theory.

AG can therefore be used as a tool to measure pathologically relevant changes in the lung and intestine. MicroPET can be used for real-time imaging of drug distribution in organs, which can visualize the interrelationship between organs. The real-time distribution of AG in the lung and intestine was consistent in our study, and changes in pathology and transcription factors in the lung and intestine confirmed that "the lung and intestine are exterior-interiorly related". These results provide an important theoretical basis for further development and application of MicroPET imaging in TCM theory in the future.

Acknowledgments

This project was financially supported by the National Natural Science Foundation of China (No.81503214), and the State Key Laboratory of Medicinal Chemical Biology (Nankai University) (No. 2018083).

Disclosure

The authors confirm that there are no conflicts of interest.

References

1 Ye X. Dong MH. A review on different English versions of an ancient classic of Chinese medicine: Huang Di Nei Jing. *J Integr Med* 2017; **15**: 11–8.
2 Fu W, Zhao J, Liu X, Gao Y, Zheng C. The roles of the TLR/NFkappaB signaling pathway in the mutual interactions between the lung and the large intestine. *Mol Med Rep* 2018; **18**: 1387–94.
3 Yin LM, Zhang GQ, Yan XK, Wang Y, Xu YD, Yang YQ. An in vivo and in vitro evaluation of the mutual interactions between the lung and the large intestine. *Evid Based Complement Alternat Med* 2013; **2013**: 695641.
4 Phelan AL, Katz R, Gostin LO. The novel coronavirus originating in Wuhan, China: challenges for Global Health governance. *JAMA* 2020; **323**: 709.
5 Wang D, Hu B, Hu C *et al*. Clinical characteristics of 138 hospitalized patients with 2019 novel coronavirus-infected pneumonia in Wuhan. *China. JAMA* 2020; **323**: 1061–1069.
6 Paules CI, Marston HD, Fauci AS. Coronavirus infections-more than just the common cold. *JAMA* 2020; **323**: 707–8.
7 Swerdlow DL, Finelli L. Preparation for possible sustained transmission of 2019 novel coronavirus: Lessons from previous epidemics. *JAMA* 2020; **323**: 1129–1130.
8 Del Rio C, Malani PN. 2019 novel coronavirus-important information for clinicians. *JAMA* 2020.**323**: 1039–1040.
9 Huang C, Wang Y, Li X *et al*. Clinical features of patients infected with 2019 novel coronavirus in Wuhan. *China. Lancet* 2020; **395**: 497–506.
10 Zhong XG, Zheng FJ, Li YH *et al*. Specific link between lung and large intestine: A new perspective on neuropeptide secretion in lung with herbal laxative stimulation. *Evid Based Complement Alternat Med* 2013; **2013**: 547837.
11 Zhang G, Jiang C, Xie N, Xu Y, Liu L, Liu N. Treatment with andrographolide sulfonate provides additional benefits to imipenem in a mouse model of Klebsiella pneumoniae pneumonia. *Biomed Pharmacother* 2019; **117**: 109065.
12 Liu L, Yan Y, Zheng L, Jia H, Han G. Synthesis and structure anti-inflammatory activity relationships studies of andrographolide derivatives. *Nat Prod Res* 2019; **34**: 782–9.
13 Zhang L, Bao M, Liu B *et al*. Effect of Andrographolide and its analogs on bacterial infection: A review. *Pharmacology* 2019;**105**: 123–134.
14 Donche S, Verhoeven J, Descamps B *et al*. The path toward PET-guided radiation therapy for Glioblastoma in laboratory animals: A mini review. *Front Med (Lausanne)* 2019; **6**: 5.

15 Matsumura A, Mizokawa S, Tanaka M *et al*. Assessment of microPET performance in analyzing the rat brain under different types of anesthesia: Comparison between quantitative data obtained with microPET and ex vivo autoradiography. *Neuroimage* 2003; **20**: 2040–50.
16 Martucci F, Pascale M, Valli MC *et al*. Impact of (18)F-FDG PET/CT in staging patients with small cell lung cancer: A systematic review and meta-analysis. *Front Med (Lausanne)* 2019; **6**: 336.
17 Chalon S, Vercouillie J, Payoux P *et al*. The story of the dopamine transporter PET tracer LBT-999: From conception to clinical use. *Front Med (Lausanne)* 2019; **6**: 90.
18 Bouter C, Bouter Y. 18F-FDG-PET in mouse models of Alzheimer's disease. *Front Med (Lausanne)* 2019; **6**: 71.
19 Molinos C, Sasser T, Salmon P *et al*. Low-dose imaging in a new preclinical total-body PET/CT scanner. *Front Med (Lausanne)* 2019; **6**: 88.
20 Jamet B, Bailly C, Carlier T *et al*. Interest of pet imaging in multiple myeloma. *Front Med (Lausanne)* 2019; **6**: 69.
21 O'Doherty J, Jauregui-Osoro M, Brothwood T *et al*. 18F-tetrafluoroborate (18F-TFB), a PET probe for imaging sodium-iodide symporter expression: Whole-body biodistribution, safety and radiation dosimetry in thyroid cancer patients. *J Nucl Med* 2017; **58**: 1666–71.
22 Cui QX, Liu Y, Zhou MG, Han YQ, Yin CC. An optimized MicroPET imaging method for the distribution and synergies of natural products. *Front Pharmacol* 2018; **9**: 948.
23 Shen F, Wu W, Zhang M *et al*. Micro-PET imaging demonstrates 3-O-beta-D-glucopyranosyl platycodigenin as an effective metabolite affects permeability of cell membrane and improves dosimetry of [(18)F]-phillygenin in lung tissue. *Front Pharmacol* 2019; **10**: 1020.
24 Qingxin C, Min F, Mengge Z *et al*. Bioactivity-based ultra-performance liquid chromatography-coupled quadrupole time-of-flight mass spectrometry for NF-kappaB inhibitors identification in Chinese medicinal preparation Bufei granule. *Biomed Chromatogr* 2016; **30**: 1184–9.
25 Shao X, Niu R, Jiang Z, Sha X, Wang Y. Role of PET/CT in management of early lung adenocarcinoma. *AJR Am J Roentgenol* 2020; **214**: 437–45.
26 Sibille L, Seifert R, Avramovic N *et al*. (18)F-FDG PET/CT uptake classification in lymphoma and lung cancer by using deep convolutional neural networks. *Radiology* 2020; **294**: 445–52.
27 Devantier L, Hansen AK, Molby-Henriksen JJ *et al*. PET visualized stimulation of the vestibular organ in Meniere's disease. *Front Neurol* 2020; **11**: 11.
28 Kandanur SGS, Tamang N, Golakoti NR, Nanduri S. Andrographolide: A natural product template for the generation of structurally and biologically diverse diterpenes. *Eur J Med Chem* 2019; **176**: 513–33.
29 Kumar G, Singh D, Tali JA, Dheer D, Andrographolide SR. Chemical modification and its effect on biological activities. *Bioorg Chem* 2019; **95**: 103511.
30 Liu W, Shan LP, Dong XS, Liu XW, Ma T, Liu Z. Combined early fluid resuscitation and hydrogen inhalation attenuates lung and intestine injury. *World J Gastroenterol* 2013; **19**: 492–502.
31 Liu Y, Wang XY, Yang X, Jing S, Zhu L, Gao SH. Lung and intestine: A specific link in an ulcerative colitis rat model. *Gastroenterol Res Pract* 2013; **2013**: 124530.
32 Cui Q, Ma F, Tao J, Jiang M, Bai G, Luo G. Efficacy evaluation of Qingyan formulation in a smoking environment and screening of anti-inflammatory compounds. *Biomed Pharmacother* 2019; **118**: 109315.
33 Chen HW, Lin AH, Chu HC *et al*. Inhibition of TNF-alpha-induced inflammation by andrographolide via down-regulation of the PI3K/Akt signaling pathway. *J Nat Prod* 2011; **74**: 2408–13.
34 Chern CM, Liou KT, Wang YH, Liao JF, Yen JC, Shen YC. Andrographolide inhibits PI3K/AKT-dependent NOX2 and iNOS expression protecting mice against hypoxia/ischemia-induced oxidative brain injury. *Planta Med* 2011; **77**: 1669–79.
35 Dai GF, Zhao J, Jiang ZW *et al*. Anti-inflammatory effect of novel andrographolide derivatives through inhibition of NO and PGE2 production. *Int Immunopharmacol* 2011; **11**: 2144–9.
36 Kumar RK, Herbert C, Foster PS. The "classical" ovalbumin challenge model of asthma in mice. *Curr Drug Targets* 2008; **9**: 485–94.

